Union operation image processing of data cubes separately processed by different objective filters and its application to void analysis in an all-solid-state lithium-ion battery

Yuta Yamamoto[1 *], Yasutoshi Iriyama[2, 3], and Shunsuke Muto[1, 4]

[1]High Voltage Electron Microscope Laboratory, Institute for Materials and Systems for Sustainability, Nagoya University, Furo-cho, Nagoya 484-8603, Japan

[2]Department of Materials, Physics, and Energy Engineering, Nagoya University, Furo-cho, Nagoya 484-8603, Japan

[3] JST-ALCA, Chiyoda-ku, Tokyo 102-0076, Japan

[4]Advanced Measurement Technology Center, for Materials and Systems for Sustainability, Nagoya University, Nagoya 464-8603, Japan

Abstract

In this paper, we propose a smart image-analysis method suitable for extracting target features with hierarchical dimension from original data. The method was applied to three-dimensional volume data of an all-solid lithium-ion battery obtained by the automated sequential sample milling and imaging process using focused ion beam/scanning electron microscope to investigate the spatial configuration of voids inside the battery. To automatically fully extract the shape and location of the voids, three types of filters were consecutively applied: median blur filter to extract relatively larger voids, morphological opening operation filter for small dot-shaped voids, and morphological closing operation filter for small voids with concave contrasts. Three data cubes separately processed by the abovementioned filters were integrated by a union operation to the final unified volume data, which confirmed the correct extraction of the voids over the entire dimension contained in the original data.

Keyword: union operation, image analysis, data-cube analysis, void analysis, all-solid-state lithium-ion battery, Avizo fire

Introduction

Image processing is widely used in the electron-microscopy field to extract specific features of target objects from a micrograph containing rich information. One of the basic and most frequently used operations is threshold processing, which only works when the contrast of the target objects is significantly different from the other irrelevant features and the image background [1, 2]. However, this method does not correctly work unless the target objects can always be well distinguished from the surrounding background contrast level.

Additional filtering may be applied to the image to overcome this problem [3-6] before the

threshold processing. For instance, one can enhance the contrast of the objective feature by subtracting the background intensity, which can be obtained by applying a median blur filter to the original image. This method is effective especially in cases where the image includes relatively larger target features alone without smaller features because the blur filter could overlook the smaller features depending on the set parameters such as the window width to average the intensity.

Another potentially effective preprocess for the threshold processing is “morphological image processing” [7-9]. This operation is performed by dilation and/or erosion processing of an original image using a specified structure element. We have successfully determined the particle size distribution of the single atoms of gold and gold sub-nano clusters supported by alumina by applying this method [7].

The threshold processing, combined with the abovementioned preprocessing operations, offers a promising method for extracting the feature of interest in a site-selective manner from the original image if an appropriate combination is selected and applied, depending on the size, shape, and contrast of the target feature with respect to the background level. The micrograph of an actual material very often includes complicated structures over a wider range of dimensions. Therefore, applying only one filter type will likely extract only a certain dimensional range among the entire target features. In this paper, we propose a method of unifying a number of images that are separately processed by the respective filters to extract all the features of interest with hierarchical dimension.

In the present paper, a three-dimensional (3D) configuration of the voids inside an all-solid-state lithium-ion battery (LIB) deposited on a substrate was investigated using the proposed method as an application example. All-solid-state LIBs have received a fair amount of attention owing to their flame-resistant property, which is free from liquid-leak risks [10]. One of the key issues for the scaling up of all-solid-state LIBs is the development of thick electrode–solid electrolyte composite whose dense texture can effectively reduce the interfacial resistance (electrode/electrode, electrode/solid electrolyte, and solid electrolyte/solid electrolyte) inside the composite [11-15]. Void analysis hence becomes very important in developing better composite electrodes for an all-solid-state LIB. In this context, the focused ion beam/scanning electron microscope (FIB/SEM) system has recently attracted much attention because one can create 3D image data of a sample by automatic alternating operations of SEM observation and FIB cross-sectioning [16-18]. The 3D volume data thus obtained was analyzed.

Methods

The composite electrode was composed of layered rock-salt-structured crystalline electrode, $LiNi_{1/3}Co_{1/3}Mn_{1/3}O_2$[19], and NASICON-structured Li^+-conductive glass–ceramic solid electrolyte Li–Al–Ti–P–O, manufactured by Ohara Inc., with a lithium conductivity of 10^{-3} $S \cdot cm^{-1}$ at 298 K [20]. This composite electrode was prepared on a silicon substrate by aerosol deposition [21], and the

electrode worked well as an electrode material in an all-solid-state LIB [22]. The orthogonal FIB/SEM system (MI4000L, HITACHI), which operated at an accelerating voltage of 15 kV, was used for the SEM secondary electron (SE) observation, operating the annular in-lens SE detector of "Gemini column^{TM}". It is in general said desirable to select a lower accelerating voltage for better spatial resolution, though we selected this voltage because smaller dot-shaped voids can be better recognized using the edge effect of SE imaging in SEM, where higher accelerating voltages should be preferable. Nevertheless, the SEs excited by the present incident electron beam are emitted from regions with no larger than 10 nm both in lateral and vertical directions [23, 24], still small enough compared to the present sampling size demanded. The resolution of the 3D image data cube was 20.0 nm·pixel^{-1} in all axes, which was constructed by SEM images of 20.0 nm^2·pixel^{-2} taken by 1,000 slicing steps by FIB at a width of 20 nm.

All the obtained SEM images were aligned in position, the substrates at the bottom and top vacuum spaces were trimmed away, and all other operations such as filtering, image subtraction, and final union operation were done on the software framework Avizo fire (FEI^{TM} Company) for image processing, volume rendering, and 3D image reconstruction. In the present study, three image-filter types were applied, in addition to the threshold processing, followed by the union operation to integrate the separately processed images to extract the respective classes of substructures from the original dataset into a single unified image dataset. This concept is shown in Fig. 1. The three filters, namely, median blur and morphological opening/closing filters, used in this study are briefly described in the Appendix.

Results and Discussion

Figure 2 shows a typical SEM image among the images of the sample subsequently sectioned. The structure is mainly characterized by a mixture of two types of contrasts with a typical size of 1–2 μ m. The brighter contrasts correspond to the electrodes, whereas the darker contrasts correspond to the solid electrolytes, which were stacked one after another in layers on the base substrate. Voids are represented by the darkest contrasts with sometimes bright edges throughout the sample irrespective of the electrode, solid electrolyte, or any element between them.

Figure 3 shows a bird's eye view of the 3D reconstructed image data cube of the sample after alignment, trimming a part of the substrate, and trimming the vacuum region above the sample. The apparent contrasts in the structure in this figure are rescaled, but the relative contrast relationship among the electrodes, solid electrolytes, and voids are preserved. Movie 1 shows a 3D representation of Fig. 3, which presents the sequential shots of the slices and rotation of the volume. Three types of voids are then processed and consequently extracted step-by-step, depending on their sizes and characteristic contrasts with respect to the surrounding background.

The relatively larger voids were first extracted following the method shown in Figs. 4(a)–(c). The

3D median blur filter with 3 × 3 × 3 pixels^3 (voxels) was applied to the original images; this process was repeated 10 times to avoid picking up even the larger contrasts in the electrodes and solid electrolytes. The blur-filtered data cube [Fig. 4(b)] was subtracted from the original data cube [Fig. 4(a)], resulting in a larger void-extracted data cube [Fig. 4(c)] after the threshold processing. The subtracted data cubes after applying the blur filter by 2, 10, and 100 times are shown in Figs. 4(d)–(f), respectively, for comparison. The void contrast is better identified by increasing the number of iterations, and 10 iterations are practically sufficient to extract larger voids.

Figures 5(a)–(c) shows the second operation to extract the small dot-shaped voids, which exhibit brighter edge contrasts. The morphological opening filter [8, 9] was applied for this purpose. The spherical shape with a diameter of 7 pixels was chosen as the best "structuring element" (defined in the Appendix) of the filter in this case after testing several types and sizes of the element. The processed data cube [Fig. 5(b)] was subtracted from the original data cube [Fig. 5(a)] to obtain the void image, as shown in [Fig. 5(c)]. For comparison, the final void-extracted images using the spherical-shaped structuring element with diameters of 3, 7, and 11 pixels are shown in Figs. 5 (d)–(f), respectively. A smaller structuring element could overlook part of the void contrasts, whereas a larger structuring element could capture parts of the solid electrolyte areas. We therefore determined that the structuring element with a spherical shape with a 7-pixel diameter is the most suitable element in determining the appropriate threshold value in this case.

The third type of operation is shown in Figs. 6(a)–(c), which was applied to voids with concave contrasts scattered inside the solid electrolytes. The morphological closing filter was selected to extract this type of voids. The spherical shape with a diameter of 7 pixels was again chosen as the best structuring element of the processing after several trials and errors. The processed data cube [Fig. 6(b)] was subtracted from the original data cube [Fig. 6(a)], and the subtracted data cube shown in Fig. 6(c) was then threshold-processed to obtain the void image. The subtracted data cubes followed by the morphological closing filter using the spherical-shaped structuring elements with diameters of 3, 7, and 11 pixels are shown in Figs. 6(d)–(f), respectively. Because the smaller structuring element failed to capture the contrast variations of the voids while the larger structuring element captured not only the voids but also the solid electrolyte parts, the optimum structuring element was determined to have a spherical shape with a diameter of 7 pixels in the present case.

The intensity threshold value of each threshold processing shown in Figs. 4–6 was appropriately chosen by inspection to exclude the electrodes and the solid electrolytes in the void-extraction processes. Then, the voxels corresponding to the voids of interest in each data cube were selected by the threshold and thus determined. In Avizo, the set of spatial coordinates of the selected voxels is called "label data," which can be unified by repeating the loading of a data cube and its threshold setting in order. This unification process is equivalent to the union operation of the label data because the operation subsequently extends the selected coordinates to the unified dataset. By assuming the

original data as *A* and the unified label data as *B*, the image math operation can be expressed as follows:

$$A * (B == 1). \quad (1)$$

Thus, we can extract the data cube, including the coordinates of the voids alone, from the original data, where "*" is the multiplication operation of the two image intensities of the same coordinates and "== 1" is a logical operation that stands for "true." The processing series is equivalent to the following union operation of the three data cubes separately processed using different filter types into a single data cube:

$$V_{all} = V_{blurring\ filter} \cup V_{morphology\ opening\ filter} \cup V_{morphology\ closing\ filter}. \quad (2)$$

The unified data cube included the upper edge contrast, which corresponds to the volume edges in vacuum, revealed by the application of the blur and morphological opening filters. The unrealistic edge contrasts were then cut away from the data cube. A bird's eye view of the resulting 3D image data cube is shown in Fig. 7, and Movie 2 shows the 3D representation of Fig. 7.

To demonstrate the effective operation of the void extraction process, the single operation-processed data cubes before the union operation were compared, as shown in Figs. 8(a)–(c), which were processed using the median blur and morphological opening and closing filters, respectively. Movies 3–5 respectively correspond to the 3D presentations in Figs. 8(a)–(c). The resulting data cube shown in Fig. 8(a) and Movie 3 includes relatively larger voids, and the amount of voids is obviously less than that in the unified data cube shown in Fig. 3 and Movie 2. The data cubes shown in Figs. 8(b) and (c) and Movies 4 and 5 mainly include smaller voids, capillary-shaped voids, and connected voids that form a network, which were overlooked by the median filter. The volume ratio of the voids in each data cube to the total volume of the voids is listed in Table 1. Various void shapes and sizes were consequently extracted by separately and subsequently applying a single image-processing filter to the original data cube and finally unifying the resultant data cubes using the union operation. Total volume fraction of the voids with respect to the total volume of the composite amounted to as small as 0.15 vol.%, widely distributed over the entire composite, as shown in Figs. 7 and 8. The present image analysis hence suggests that further improvements of the composite electrode can be realized by the reduction of local void fractions, because the voids should play a primary role in hampering lithium-ion conduction in the composite electrode.

Conclusion

We have proposed a suite of image-processing methods to extract a target feature with a wide dimensional range from 3D volume image data. The method consists of three separate filtering operations as preprocesses of the threshold processing using the following filters: median blur, morphological opening, and morphological closing filters (where each filter effectively operates in different dimensions and contrast features), followed by the union operation to unify the three results. We demonstrated that the present method applied to investigate the spatial distribution of voids inside

an all-solid-state LIB and all the voids were successfully extracted by the union operation of the three separately processed data cubes, depending on the size and contrast of the voids. The obtained 3D configuration of the voids inside the battery is expected to provide an insight to improve its performance, e.g., the spatial distributions of the voids can be easily visualized using a color look-up table, especially the difference between the inside of the electrode/electrolyte and the interface region between the two. This subject is however beyond the scope of the present methodological report.

Acknowledgment

This work was supported in part by the Grants-in-Aid for Scientific Research on Innovative Areas "Nano Informatics" (No. 25106004) and in part by Kiban-kenkyu A (No. 26249096) from the Japan Society of the Promotion of Science.

Appendix: Brief descriptions of the image filters used in the present study

The following three filters were used in the preprocessing methods applied in the present study:

(i) Median blur filter

This filter replaces the pixel intensity value with the median value among the specified neighboring area that centers the selected pixel. This process is performed to average the image contrast by repeated operations.

(ii) Morphological opening filter

(iii) Morphological closing filter

Each of the filters in (ii) and (iii) is applied in two consecutive basic operations, namely, dilation and erosion, where the morphological opening filter is first applied in the erosion operation followed by dilation. The morphological closing filter is first applied in the dilation operation followed by erosion.

A binary subset image with a simple shape, called the "structuring element," is first defined, and it probes the image of interest to determine how the structuring element fits or misses the shapes in the image. Now, we let X and Y be the original image and structuring elements, respectively, where Y is an open disk with radius r centered at the origin. The dilation of X by Y, denoted as $X \oplus Y$, is defined as

$$X \oplus Y = \cup_{y \in Y} (X + y), \tag{A-1}$$

where y is an arbitrary vector inside Y. This operation is understood as the locus of the points covered by Y when the center of Y moves inside X. On the other hand, the erosion of X by Y, denoted as $X \ominus Y$, is defined as

$$X \ominus Y = \cup_{y \in Y} (X - y), \tag{A-2}$$

which is understood in the same manner as the locus of points reached by the center of

Y when *Y* moves inside *X*. The above basic operations are shown in the upper row in Fig. A-1.

The opening operation results in the locus of translations of structuring element *Y* inside image *X*. In case the structuring element is a square with a side of 10 units in length and a disk with a radius of 2 units (pixels), the resultant feature is a square with a side of 10 units in length with rounded corners, where the corner radius is 2 units. This operation mostly retains the shape and size of the target object if the radius of the structuring element is smaller than the largest dimension of the target object, whereas it merges the object to the background if the radius of the structuring element is larger than the largest dimension of the target object.

On the other hand, closing is a complement of the locus of translations of the symmetry of the structuring element outside image *X*. This operation connects the objects separated from one another by a distance smaller than the diameter of the structuring element. The situations are shown in the bottom row in Fig. A-1.

References

1. Prewitt J M S and Mendelsohn M L (1966) The analysis of cell images. *Ann. Acad. Sci.* 128: 1035-1053.

2. Otsu N (1979) A threshold selection method from gray-level histograms. *IEEE Trans. Systems Man Cybernet* 9: 62-66.

3. Piccardi M (2004) Background subtraction techniques. *IEEE International Conference on Systems, Man and Cybernetics* 4: 3099-3104.

4. Bele P, Jager F, and Stimming U (2007) Image processing for TEM micrographs of platinum nanoparticles on glassy carbon. *Micro. and Anal. Nanotech. Sup.* S5-S7.

5. Lohr C, Kunding A H, Bhatia V K, and Stamou D (2009) Constructing size distributions of liposomes from single-object fluorescence measurements. *Method in Enzymology,* 465: 143-160.

6. Iwabuchi S, Kakazu Y, Koh J Y, and Harata C (2013) Evaluation of the effectiveness of Gaussian filtering in distinguishing punctate synaptic signals from background noise during image analysis. *Journal of Neuroscience Methods* 223: 92-113.

7. Yamamoto Y, Arai S, Esaki A, Ohyama J, Satsuma A, and Tanaka N (2014) Microscopy 63: 209-218.

8. Haralick R M, Sternberg S R, and Zhang X (1987) Image analysis using mathematical morphology. *IEEE Trans. Pattern Anal. Mach. Intell.* 9: 532–550.

9. Edward R D and Roberto A L (2003) Hands-on morphological image processing. *Society of Photo-Optical Instrumentation Engineers,* pp. 1-88: 101-178.

10. Kobayashi E, Plashnitsa L S, Doi T, Okada S, and Yamaki J (2010) Electrochemical properties of

Li symmetric solid-state cell with NASICON-type solid electrolyte and electrodes. *Electrochemistry Communications* 12: 894-896.

11. Aboulaich A, Bouchet R, Delaizir G, Seznec V, Tortet L, Morcrette M, Rozier P, Tarascon J M, Viallet V, and M. Dolle (2011) A new approach to develop safe all-inorganic monolithic Li-Ion batteries. *Advanced Energy Materials.* 1: 179-183.

12. Kamaya N, Homma K, Yamakawa Y, Hirayama M, Kanno R, Yonemura M, Kamiyama T, Kato Y, Hama S, Kawamoto K, and Mitsui A (2011) A lithium superionic conductor. *Nature Materials* 10: 682-686.

13. Ohta S, Komagata S, Seki J, Saeki T, Morishita S, and Asaoka T (2013) All-solid-state lithium ion battery using garnet-type oxide and Li3BO3 solid electrolytes fabricated by screen-printing. *Journal of Power Sources* 238: 53-56.

14. Wei T, Gong YH, Zhao X, and Huang K (2014) An all-ceramic solid-state rechargeable Na^{+}-battery operated at intermediate temperatures. *Advanced Functional Materials* 24: 5380-5384.

15. Iwasaki S, Hamanaka T, Yamakawa T, West W C, Yamamoto K, Motoyama M, Hirayama T, and Iriyama Y (2014) Preparation of thick-film $LiNi_{1/3}Co_{1/3}Mn_{1/3}O_2$ electrodes by aerosol deposition and its application to all-solid-state batteries. *Journal of Power Sources* 272: 1086-1090.

16. Drobne D, Milani M, Zrimec A, Leser V, and Zrimec M B (2005) Electron and ion imaging of gland cells using the FIB/SEM system. *Journal of Microscopy* 219: 29-35.

17. Bhandari Y, Sarkar S, Groeber M, Uchic M D, Dimiduk D M, and Ghosh S (2007) 3D polycrystalline microstructure reconstruction from FIB generated serial sections for FE analysis. *Computational Materials Science* 41: 222-235

18. Drobne D, Milani M, Leser V, Tatti F, Zrimec A, Znidarsic N, Kostanjsek R, and Strus J (2008) Imaging of intracellular spherical lamellar structures and tissue gross morphology by a focused ion beam/scanning electron microscope (FIB/SEM). *Ultramicroscopy* 108: 663-670

19. Ohzuku T and Makimura Y (2001) Layered lithium insertion material of $LiCo_{1/3}Ni_{1/3}Mn_{1/3}O_2$ for lithium-ion batteries. *Chemistry Letters* 7: 642-643.

20. J. Fu (1997) Fast Li^{+} ion conduction in Li_2O-Al_2O_3-TiO_2-SiO_2-P_2O_5 glass-ceramics. *Journal of the American Ceramic Society* 80: 1901-1903.

21. Akedo J (2006) Aerosol deposition of ceramic thick films at room temperature: Densification mechanism of ceramic layers. *J. Am. Ceram. Soc.* 89: 1834-1839.

22. Kato T, Iwasaki S, Yamakawa T, Ishiii Y, Motoyama M, West WC, and Iriyama Y (2015) Preparation of thick-film electrode-solid electrolyte composites combined with $Li_7La_3Zr_2O_{12}$ and their electrochemical properties. submitted for publication.

23. Seiler H (1983) Secondary electron emission in the scanning electron microscope. *Journal of Applied Physics* 54: R1-R18.

24. Inada H, Su D, Egerton R F, Konno M, Wu L, Ciston J, Wall J, and Zhu Y (2010) Atomic

Imaging Using Secondary Electrons in a Scanning Transmission Electron Microscope : Experimental Observations and Possible Mechanisms. *Ultramicroscopy* 110: 1-20

Figure captions

Fig. 1 Schematic diagram of (top figure) the conventional and (bottom) the new processes proposed in the present study for extracting voids from a 3D data cube.

Fig. 2 Typical SEM image of the sample.

Fig. 3 Bird's eye view of the data cube in an all-solid-state LIB. All SEM images are aligned and reconstructed to a 3D image data cube, and the base substrate and top vacuum region are then trimmed away.

Fig. 4 Demonstration on how the blur filter extracts larger voids. (a) Part of a data cube showing relatively larger void contrasts. (b) Image after the application of median blur filter to the area in (a). (c) Resultant image obtained by the image arithmetic in (a) and (b). (d)–(f) Demonstration on how the resultant difference image changes with 2, 10, and 100 times of iteration during the 3D median filtering, respectively.

Fig. 5 Demonstration on how the opening filter extracts smaller voids. (a) Part of the image containing smaller dot-shaped void contrasts. (b) Image after the application of morphological opening filter to the area in (a). (c) Resultant image obtained by the image arithmetic in (a) and (b). (d)–(f) Resultant void-extracted images using the spherical-shaped structuring element with diameters of 3, 7, and 11 pixels, respectively.

Fig. 6 Demonstration on how the closing filter extracts the voids with concave contrasts inside the solid electrolyte. (a) Part of the image containing concave void contrasts. (b) Image after the application of morphological closing filter to the area in (a). (c) Resultant image obtained by image arithmetic of (a) and (b). (d)–(f) Resultant void-extracted images using the spherical-shaped structuring element with diameters of 3, 7, and 11 pixels, respectively.

Fig. 7 Three-dimensional configuration of all voids inside the all-solid-state LIB extracted from the original data cube (Fig. 3) using the present method.

Fig. 8 Comparison among the data cubes separately processed by respective single filters. (a) Data cube processed by the median blur filter. (b) Data cube processed by the morphological opening filter. (c) Data cube processed by the morphological closing filter.

Fig. A-1 Conceptual illustration of the (top) morphological image processing methods and (bottom)opening/closing operations.

Table 1. Volume ratio of the voids in each processed data cube to the total void volume.

Table 1. Volume ratio of the voids in each processed data cube to the total void volume.

	Median blur	Morphological opening	Morphological closing
Volume ratio to total void volume	52.5%	59.9%	17.9%

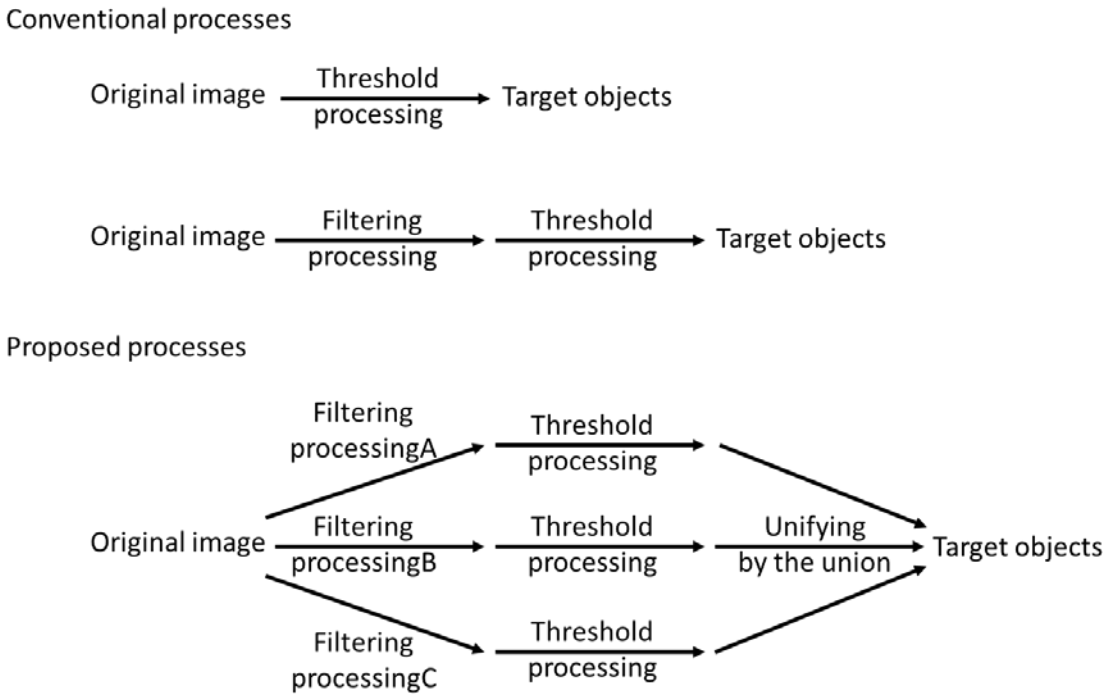
Conventional processes
Original image
Threshold processing
Target objects
Original image
Filtering processing
Threshold processing
Target objects
Proposed processes
Original image
Filtering processingA
Filtering processingB
Filtering processingC
Threshold processing
Threshold processing
Threshold processing
Unifying by the union
Target objects

Fig. 1

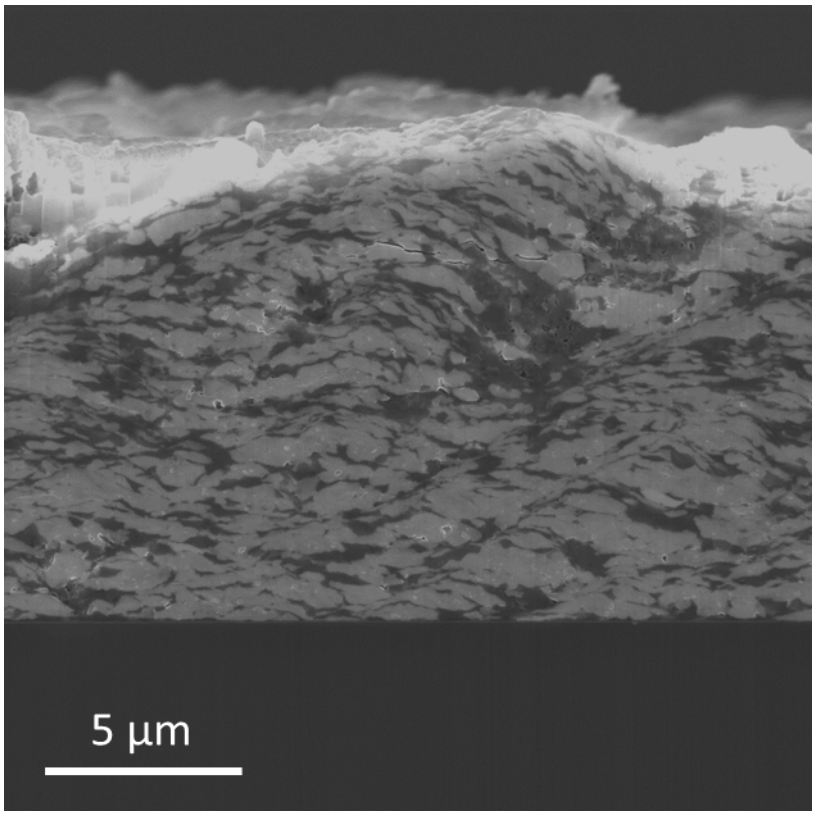

Fig. 2

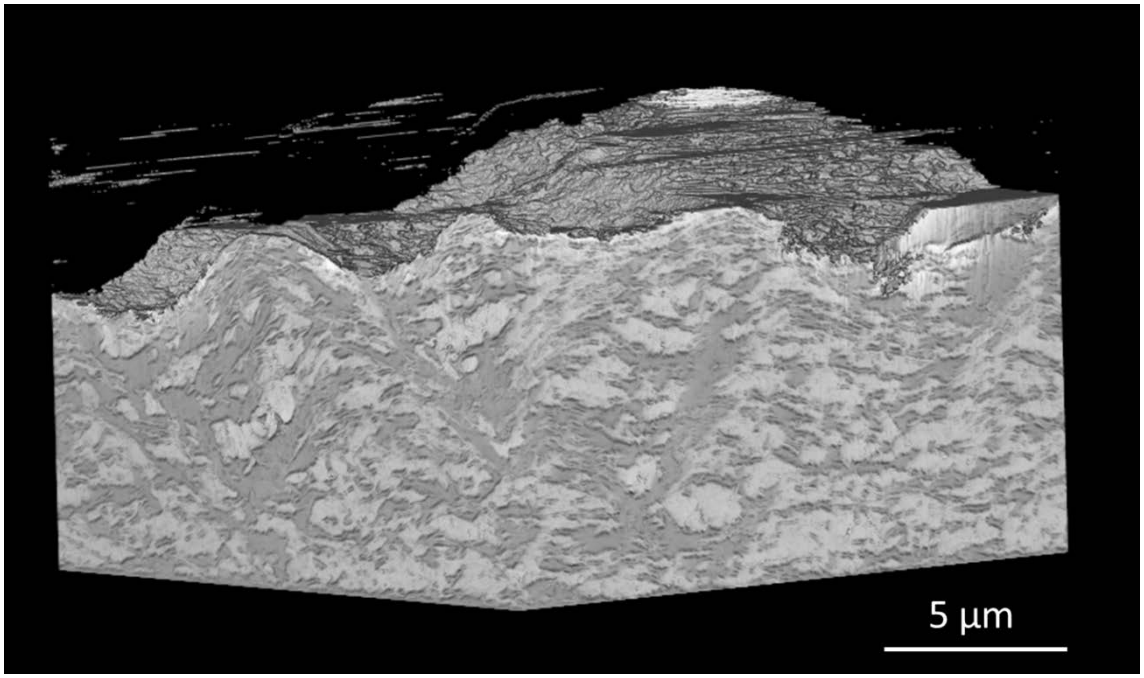

Fig. 3

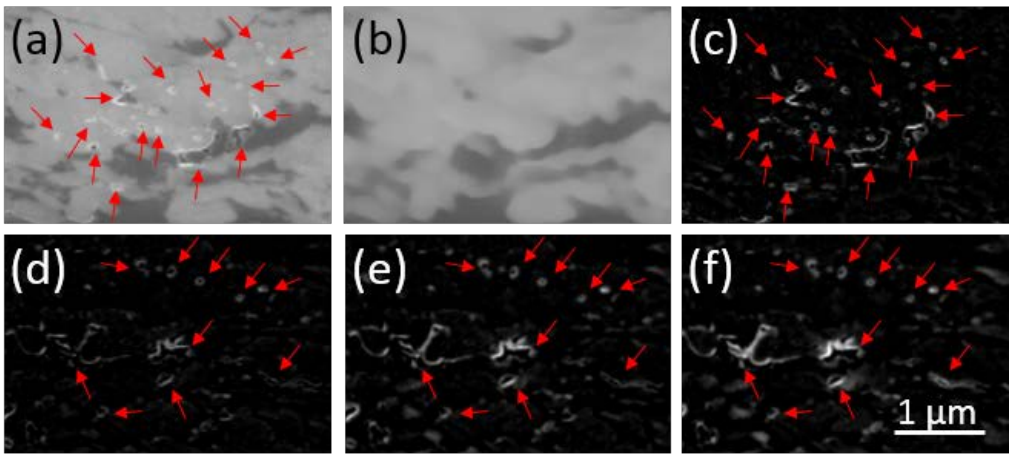

Fig. 4

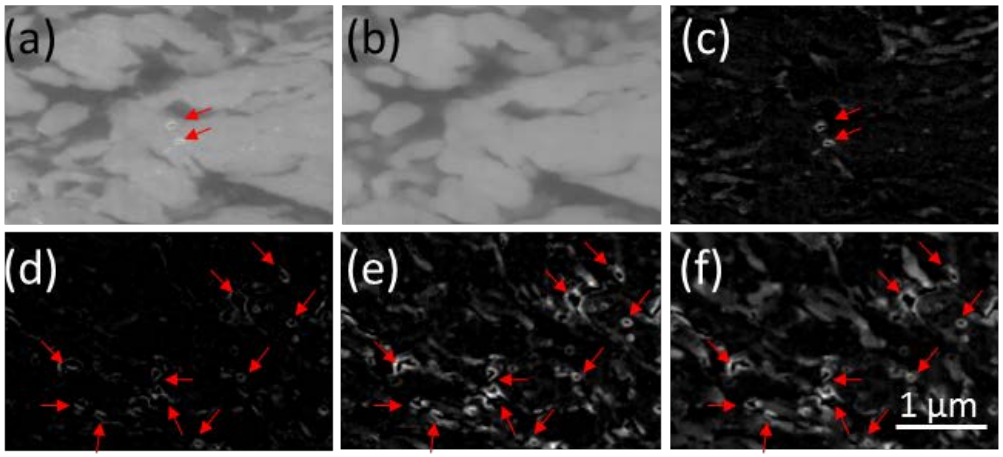

Fig. 5

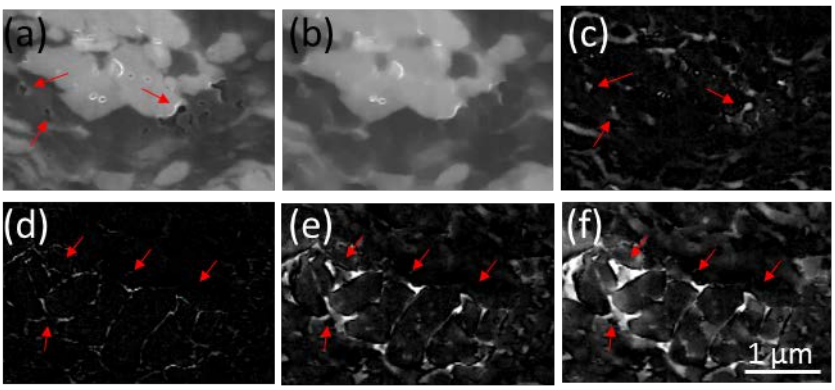

Fig. 6

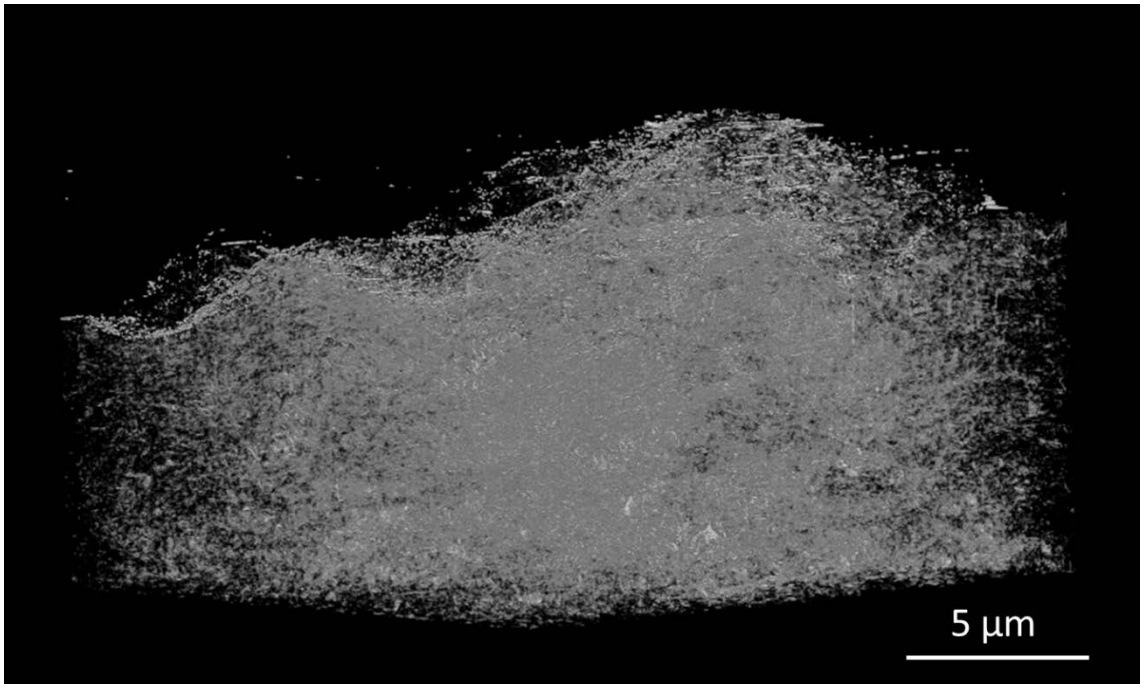

Fig. 7

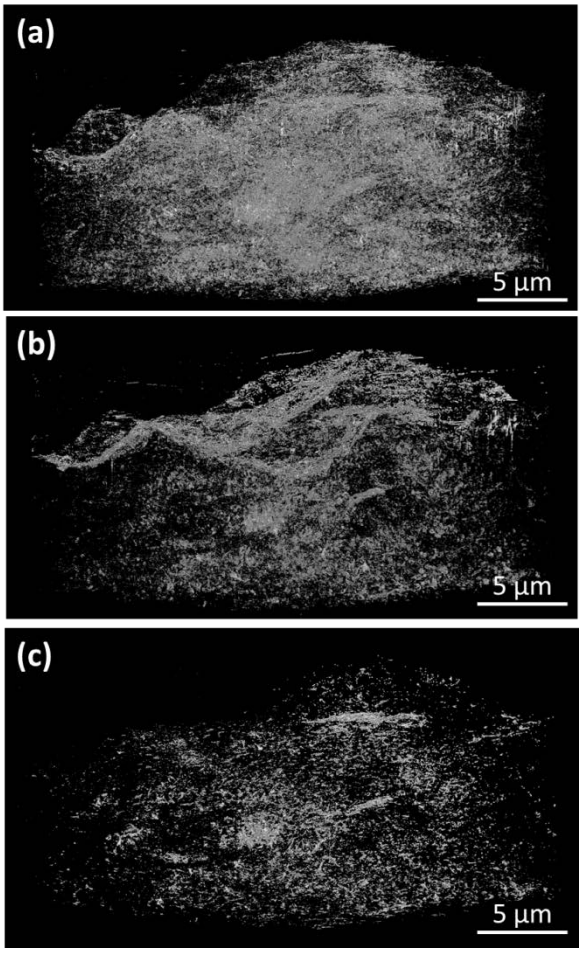

Fig. 8

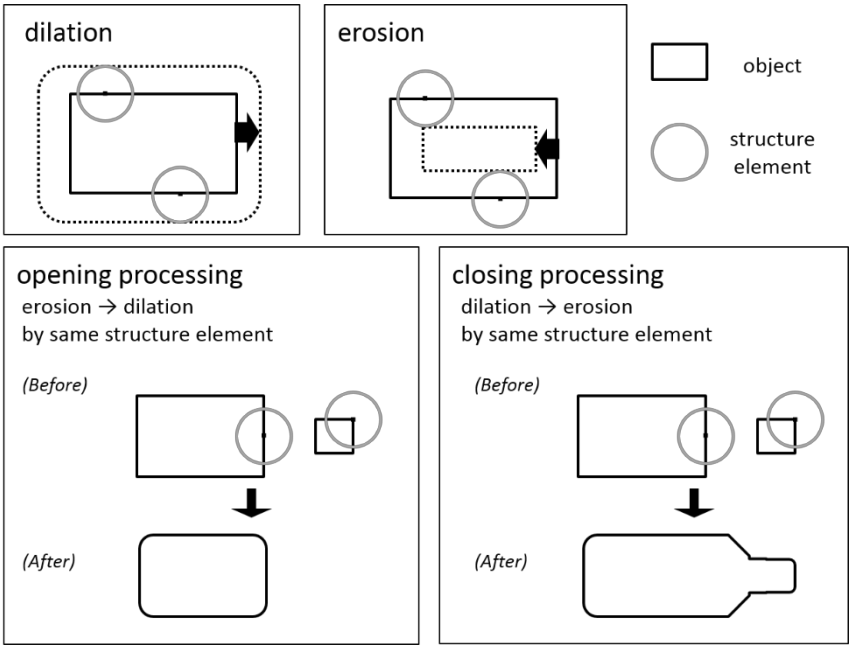
dilation
erosion
object
structure element
opening processing
erosion → dilation
by same structure element
(Before)
(After)
closing processing
dilation → erosion
by same structure element
(Before)
(After)

Fig. A-1